

2021-12

Seasonal sea ice persisted through the Holocene Thermal Maximum at 80N

Pienkowski, AJ

<http://hdl.handle.net/10026.1/17349>

10.1038/s43247-021-00191-x

Communications Earth & Environment

Springer Science and Business Media LLC

All content in PEARL is protected by copyright law. Author manuscripts are made available in accordance with publisher policies. Please cite only the published version using the details provided on the item record or document. In the absence of an open licence (e.g. Creative Commons), permissions for further reuse of content should be sought from the publisher or author.

Seasonal sea ice persisted through the Holocene Thermal Maximum at 80°N

Anna J. Pieńkowski¹  [✉], Katrine Husum¹ , Simon T. Belt² , Ulysses Ninnemann³ , Denizcan Köseoğlu², Dmitry V. Divine¹, Lukas Smik², Jochen Knies^{4,5}, Kelly Hogan⁶  & Riko Noormets⁷

The cryospheric response to climatic warming responsible for recent Arctic sea ice decline can be elucidated using marine geological archives which offer an important long-term perspective. The Holocene Thermal Maximum, between 10 and 6 thousand years ago, provides an opportunity to investigate sea ice during a warmer-than-present interval. Here we use organic biomarkers and benthic foraminiferal stable isotope data from two sediment cores in the northernmost Barents Sea (>80 °N) to reconstruct seasonal sea ice between 11.7 and 9.1 thousand years ago. We identify the continued persistence of sea-ice biomarkers which suggest spring sea ice concentrations as high as 55%. During the same period, high foraminiferal oxygen stable isotopes and elevated phytoplankton biomarker concentrations indicate the influence of warm Atlantic-derived bottom water and peak biological productivity, respectively. We conclude that seasonal sea ice persisted in the northern Barents Sea during the Holocene Thermal Maximum, despite warmer-than-present conditions and Atlantic Water inflow.

¹Norwegian Polar Institute, Fram Centre, N-9296 Tromsø, Norway. ²Biogeochemistry Research Centre, School of Geography, Earth and Environmental Sciences, University of Plymouth, Plymouth PL4 8AA, UK. ³Department of Earth Science and Bjerknes Centre for Climate Research, UiB University of Bergen, N-5007 Bergen, Norway. ⁴Geological Survey of Norway, NO-7491 Trondheim, Norway. ⁵Centre for Arctic Gas Hydrate, Environment and Climate, Department of Geosciences, UiT- The Arctic University of Norway in Tromsø, N-9037 Tromsø, Norway. ⁶British Antarctic Survey, NERC, High Cross, Cambridge CB3 0ET, UK. ⁷Department of Arctic Geology, The University Centre in Svalbard (UNIS), N-9171 Longyearbyen, Svalbard, Norway. ✉email: Anna.Pienkowski@npolar.no

The dramatic decline in Arctic sea ice over recent decades represents one of the most poignant signs of contemporary, anthropogenically forced climatic change¹. This loss raises considerable concerns for environments, ecosystems and communities at both regional and global scales because of the pivotal role that sea ice plays in the Earth's climate system via energy budgets, feedback loops, atmosphere–ocean exchange and oceanographic circulation^{1,2}. Accordingly, the consequences of Northern Hemisphere sea-ice loss will cascade through the Earth System, thereby impacting lower latitudes, for example via changing atmospheric circulation and more frequent extreme weather events³. The detailed response of sea-ice cover to, and its role in, an increasingly warmer future climate remains uncertain, however, as numerical-model-based future projections vary considerably between regions and different models^{4–6}. For example, a winter ice-free Barents Sea is projected by 2061–2088, but there is considerable spread between model-based sea-ice extent projections for the next few decades, for instance ranging from 0.1 (GFDL CM3 model) to 0.6×10^6 km² (NorESM1-M) for the winter of 2030⁶. Similarly, CMIP5 model simulations of the timing of an ice-free Arctic Ocean vary from the 2010s to the late 2070s, depending on the model used⁴. Such variability in model-based forecasts stems from differences in parametrization, model approaches, and future emission scenarios^{6,7}, but is also attributable to the inherent complexities of internal climate variability. At present, these factors limit the accuracy of future projections^{4,8}.

While model simulations offer some insight into potential future sea-ice states in the Arctic, geological archives provide critical information on how sea ice responded to substantial climatic warming in the past, especially during periods characterized by warmer-than-present conditions. Detailed sea-ice histories documenting longer term variability past the observational period thus contribute significantly to the understanding of underlying causes and the contextualization of recent and potential future changes. Such a longer term, palaeo aspect is particularly relevant considering the current trend towards a warmer global climate in tandem with Arctic amplification⁹. The early Holocene Barents Sea provides a unique opportunity to study Arctic sea ice during the most recent past warm period in an oceanographically dynamic area that serves as a focus for Arctic–Atlantic Ocean interaction⁷ and that has been identified as a hotspot for current Arctic warming¹⁰. Here, we present the first high-resolution, decadal-scale early Holocene sea-ice reconstruction from the high Arctic Barents Sea from two sites (Fig. 1) based on the sea-ice proxy IP₂₅ and other biomarkers, alongside foraminiferal stable isotopes ($\delta^{18}\text{O}$, $\delta^{13}\text{C}$). Our reconstructions unequivocally demonstrate that, despite warm climatic conditions and Atlantic Water influence, seasonal sea ice persisted throughout the early Holocene (up to ~9.1 cal ka BP) in the northern Barents Sea at the border to the Arctic Ocean. We further show that high biological productivity characterized this region during that time, with sporadic phytoplankton blooms occurring along the Marginal Ice Zone (MIZ). Our results raise important questions about the response to, and long-term fate of, Arctic sea ice in an increasingly warming climate, in a region of high climatic, environmental and economic importance.

Results and discussion

Seasonal sea ice persists throughout the warm early Holocene.

Our reconstructions reveal the continued persistence of seasonal sea ice during the early Holocene in the northern Barents Sea, evidenced by the continuous occurrence of the sea-ice biomarkers IP₂₅ and IPSO₂₅ in both investigated cores (Fig. 2). Both these sympagic biomarkers show elevated concentrations following the Younger

Dryas cold period (YD, 12.9–11.7 cal ka BP) and into the early Holocene, until ~9.1 cal ka BP, when their concentrations begin to decline. This pattern is also mirrored in the two biomarkers produced by open-water phytoplankton, HBI III and HBI IV, which display peak concentrations at 11.7–9.1 cal ka BP and decrease thereafter (Fig. 2). Further, by combining IP₂₅ concentrations with those of the pelagic biomarker HBI III (see 'Methods'), we identify predominantly intermediate (i.e. 10–50%; sea-ice categories sensu Köseoglu et al.¹¹, see 'Methods') spring sea-ice concentrations (SpSIC) following the YD, until ~9.1 cal ka BP (Figs. 2 and 3). Both sites in the northern Barents Sea have similar SpSIC trends during the period 11.7–9.1 cal ka BP, although 06GC shows slightly higher sea-ice concentrations (~20–55%) compared to the more northerly 11GC (~10–40%). Sea ice increases at both sites after ~9.1 cal ka BP, shifting from intermediate to predominantly extensive (i.e., >50%) by ~8.3 cal ka BP (Fig. 2).

The orbitally forced summer insolation maximum during the Holocene Thermal Maximum (HTM, ~10–6 ka BP) resulted in warmer air and ocean temperatures globally at that time¹², though these signals may have been primarily seasonally driven¹³. At higher latitudes, increased temperatures may have also acted as an effective mechanism to thin sea ice and/or reduce its extent by lowering albedo in a positive feedback loop^{14,15}. At 80°N, mean insolation increased by 5 W m^{-2} (annual) or $\sim 50 \text{ W m}^{-2}$ (June) compared to present¹⁶ (Fig. 3). Although the predominantly intermediate SpSIC seen in our two archives is consistent with a warm period, our results nonetheless show that the northern Barents Sea was never entirely free from seasonal sea ice at this time.

Across the Barents Sea–Svalbard region, marine geological archives also suggest markedly warmer conditions beginning ~11 cal ka BP. This is considered to be tied to the concomitant northward inflow of relative warm and saline Atlantic waters from the south^{17–20} following deglaciation and the YD, even if model simulations vary in the exact timing of the recovery of the AMOC (Atlantic meridional overturning circulation)^{21,22}. The warm signal is especially prominent along the western margin of Spitsbergen, where benthic foraminiferal transfer functions suggest some of the highest bottom water temperatures of the Holocene at 11.5–8.2 cal ka BP²³. Additionally, molluscs collected from glacio-isostatically uplifted shorelines show that warm water faunas including *Mytilus edulis* (blue mussel) inhabited the northwestern coast of Svalbard during the HTM²⁴. An overall warmer early Holocene climate is also revealed by terrestrial data across the Svalbard archipelago, suggesting smaller glacier extents and higher air temperatures²⁵ (Fig. 3), as well as minimal sea ice covering the fjords²⁶.

Many other marine archives across the Barents Sea–Svalbard region imply drastically reduced sea ice, if not completely open water conditions, during the early Holocene^{23,27–30}. For example, biomarker profiles from Fram Strait, west of Svalbard, mimic the individual HBI patterns seen in our two archives (Fig. 2), with high concentrations of IP₂₅ during the YD, before declining in the early Holocene, when elevated brassicasterol levels point to high phytoplankton productivity²⁷. Nevertheless, considerable regional variability exists, not least in the northern Barents Sea where existing records are complicated by scarce or low-resolution Holocene sediments^{31,32} and chronological issues³³. The only other HBI-based record in the vicinity of our two sites commences at 9.5 cal ka BP²⁹ (Fig. 1), thus overlapping with our archives by 500 cal a. Even so, the lower part of that archive²⁹ shows IP₂₅ and HBI III concentrations on a par with our individual profiles of these two biomarkers, as well as confirming the early Holocene peak in HBI III (Fig. 2). Other relevant studies south of our sites (Fig. 1) show differing reconstructions depending on the proxy method used. Dinoflagellate-cyst-based

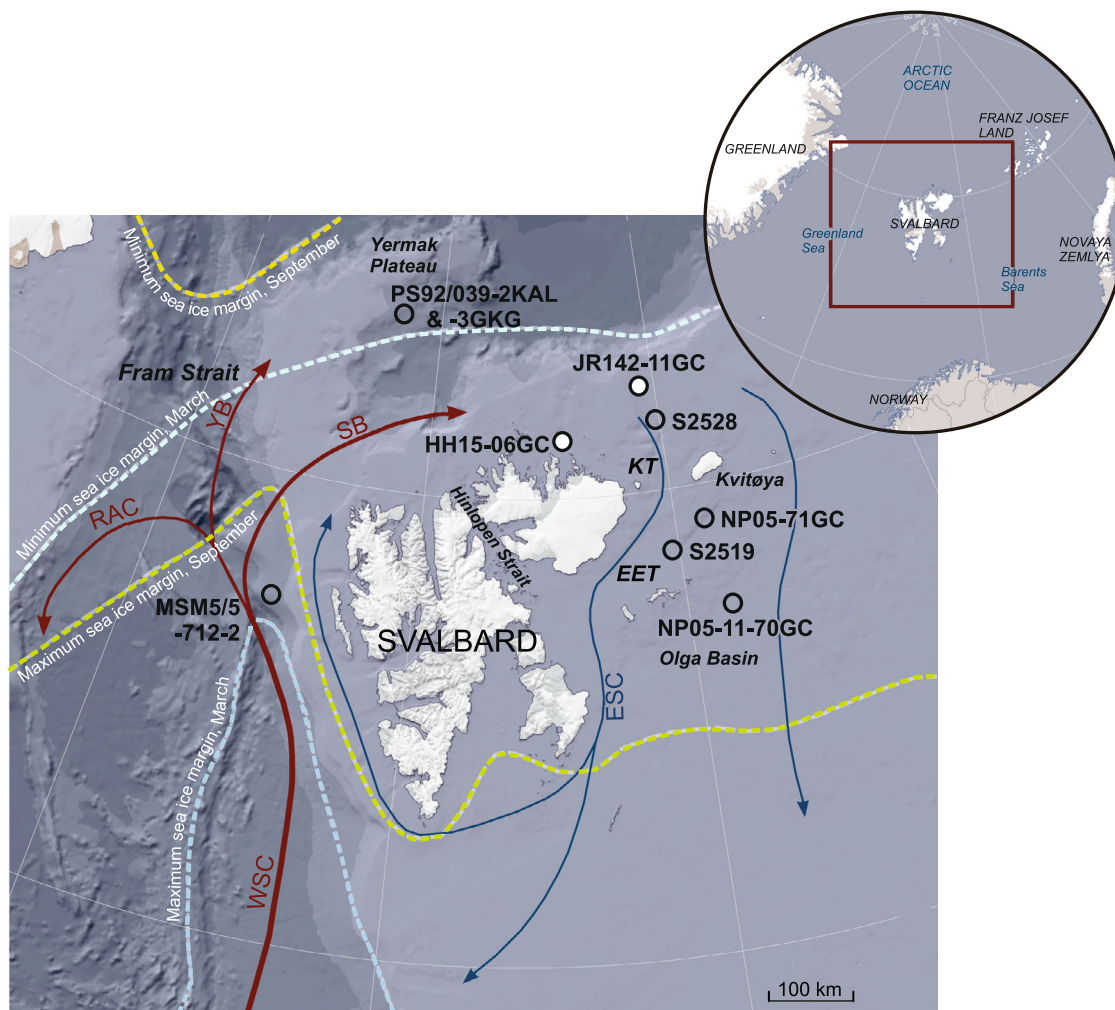


Fig. 1 Map of study area, showing modern oceanography and sea-ice extent. Sites for cores 11GC (JR142-11GC; 81°04.90'N 28°55.60' E, 359 m water depth) and 06GC (HH15-06GC; 80°32.60'N, 23°31.40' E, 320 m water depth) are indicated by white circles. Other relevant cores discussed in the text are shown by black unfilled circles: MSM5/5-712-2²⁷ in eastern Fram Strait; PS92/039-2KAL and PS92/039-3GKG³² on the Yermak Plateau; S2528^{33,34} in Kvitøya Trough; S2519³³ in Erik Eriksen Trough; NP05-71GC²⁰ south of Kvitøya; and NP05-11-70GC²⁹ in Olga Basin. Dashed lines show the average minimum and maximum sea ice margins for March (minimum: ice blue, maximum: light blue) and September (minimum: yellow, maximum: light green) in the period 1985–2014⁷⁷. KT and EET denote the Kvitøya Trough and Erik Eriksen Trough, respectively. The red arrow shows the Atlantic-sourced West Spitsbergen Current (WSC), which winds its way northward and splits into the Svalbard Branch (SB), Yermak Branch (YB), and the Return Atlantic Current (RAC). The blue arrow represents the Arctic Ocean-sourced East Spitsbergen Current (ESC).

Modern Analogue Technique transfer functions suggest 8–10 months of sea-ice cover per year at ~11.3–8.7 cal ka BP³⁴ while benthic foraminifera in the same and a nearby core (S2825 and S2519, respectively) show pronounced peaks in taxa indicative of bioproductivity and Atlantic Water inflow³³. Conversely, biogenic proxies (benthic foraminifera assemblages, planktic foraminifera and foraminiferal stable isotopes) in a nearby marine archive (NP05-71GC) suggest reduced sea ice, warm surface water conditions, and a strong inflow of Atlantic Water at 11.7–8.6 cal ka BP²⁰.

Regional variability is also evident in our reconstructed records (Figs. 2 and 3). The northern site (11GC) exhibits lower SpSIC compared to the southern site (06GC), with the latter occasionally showing extensive (>50%) SpSIC. This may be a result of 06GC being affected by fast ice anchored to the nearby Svalbard coast and/or meltwater off Svalbard promoting sea-ice formation, even if meltwater influence would have been considerably diminished by the early Holocene compared to deglaciation in the late Pleistocene³⁵. However, the differences in SpSIC may also be a function of the variable influence of Atlantic Water at the two

core sites, with changes in direction and magnitude of subsurface inflow during this time. Benthic foraminiferal oxygen stable isotopes ($\delta^{18}\text{O}$) in 06GC are high during the early Holocene (ca. 5‰; Fig. 3), whereas the more northerly core 11GC shows slightly lower values (ca. 4.8‰) and a 2-step increasing trend, which may explain the difference in SpSIC between the two sites (Fig. 3). Since the $\delta^{18}\text{O}$ signal (of calcifiers) in the modern Barents Sea is primarily driven by temperature rather than salinity^{36,37}, bottom waters may have been slightly warmer at the more northerly site during the HTM. At the same interval in core 06GC we also observe the benthic foraminiferal species *Cassidulina neoteretis* (K. Husum, personal observation 2020), an indicator of Atlantic Water^{38,39} often found in stratified settings^{40,41}. Collectively with the stable isotopes, this suggests that Atlantic-derived bottom water reached both sites during the early Holocene, similar to south of Kvitøya where a contemporaneous record²⁰ shows comparable benthic $\delta^{18}\text{O}$ values. A strong Atlantic Water influence (below the pycnocline at ~100 m water depth) is also exerted on the west Svalbard shelf during this time²³. The presence of sea ice throughout the HTM at both our sites, as

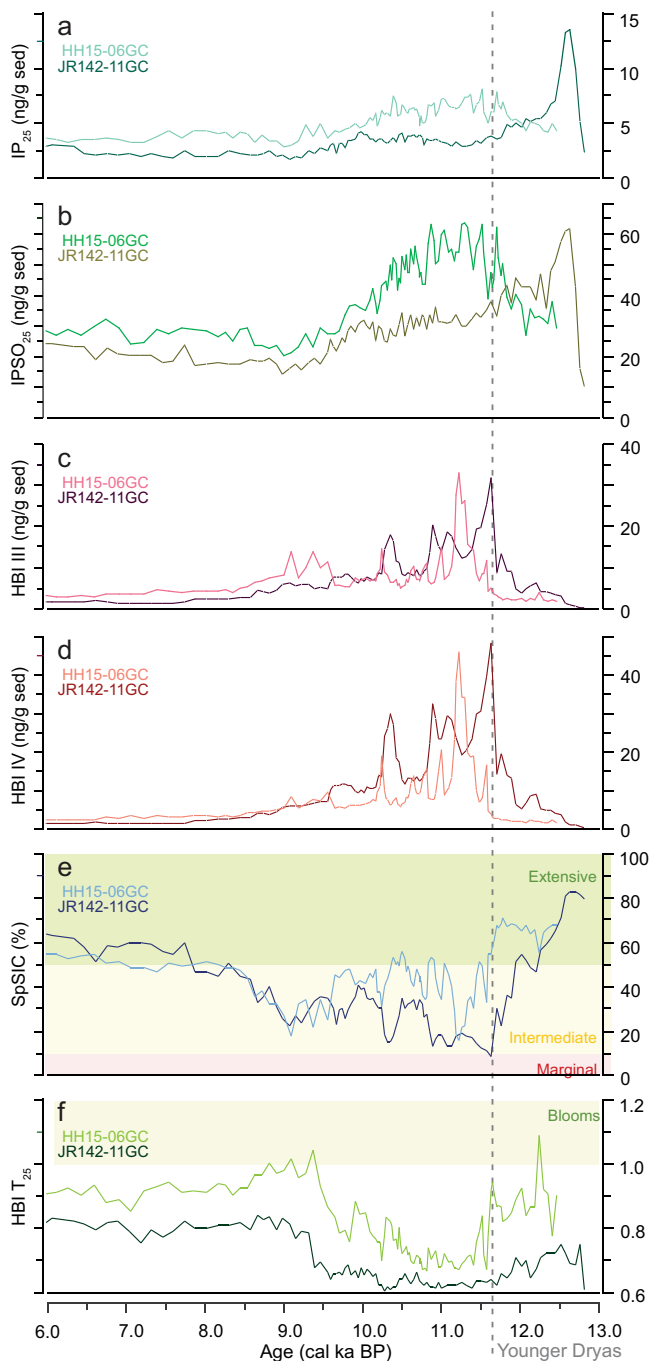


Fig. 2 Biomarker results from cores 11GC (JR142-11GC) and 06GC (HH15-06GC), from the Younger Dryas to 6 cal ka BP. **a–d** Individual concentrations of HBI (highly branched isoprenoid) biomarkers: **a** sea-ice biomarker IP₂₅; **b** sea-ice biomarker IPSO₂₅; **c** pelagic biomarker HBI III; **d** pelagic biomarker HBI IV. **e, f** Ratio-based reconstructions (see ‘Methods’ for details) of: **e** concentrations of spring sea-ice cover (SpSIC %), and **f** phytoplankton blooms along the Marginal Ice Zone (HBI T₂₅).

indicated by biomarker data presented herein, argues against Atlantic Water occupying the whole water column, however (as suggested on the western Svalbard margin after 9.6 cal ka BP²³), because its heat tends to hinder sea-ice formation³⁷. It is therefore likely that the bottom Atlantic Water was overlain by an intermediate, Arctic-derived layer and sea-ice-related halocline, as it is today⁴², with limited vertical mixing occurring⁴³.

Early Holocene characterized by high biological productivity and Atlantic Water influence. Individual profiles of the pelagic diatom-derived biomarkers HBI III and HBI IV in our two northern Barents Sea archives reveal that open-water biological productivity likely reached a maximum during the early Holocene (Fig. 2), following a period of much reduced productivity during the YD, probably as a result of the contrasting sea-ice conditions. This early Holocene phytoplankton productivity, while elevated, may have rarely reached the particularly high levels seen in the modern Barents Sea MIZ⁴⁴, however. The HBI T₂₅ index, a ratio between HBI III and HBI IV (see ‘Methods’), has recently been proposed as a potential proxy for the spring diatom bloom, on the basis of its strong association with spring chlorophyll-a⁴⁴. In our two archives, HBI T₂₅ values are mostly below the threshold of phytoplankton blooming at the MIZ (defined⁴⁴ as spring chlorophyll-a >1.5 mg m⁻³), indicating the absence of spring blooms in 11GC (all HBI T₂₅ < 1), with sporadic blooms (i.e., HBI T₂₅ > 1) at the 06GC site during the YD and around 9.3 cal ka BP (Fig. 2). Nevertheless, our average HBI III concentrations within the early Holocene at 11.7–9.1 cal ka BP (06GC: 9.3 ng g⁻¹; 11GC: 11.1 ng g⁻¹) are similar to the mean modern value from the Barents Sea MIZ based on surface sediments⁴⁵ (12.9 ng g⁻¹). A productive early Holocene sea-ice edge with intermediate SpSIC is further supported by the relatively low endobenthic foraminiferal δ¹³C values in both records (Fig. 3). Lower δ¹³C values at 06GC compared to 11GC are suggestive of more favourable conditions farther south, which could be due to increased climatic amelioration and/or proximity to the northern Svalbard coasts bringing additional nutrients and mixing to the water column.

High pelagic productivity during the early Holocene has been observed elsewhere across the Barents Sea²⁸ and adjacent regions⁴⁶, including off northern Norway⁴⁷ and in eastern Fram Strait²⁷. Warm-water (Atlantic-affiliated) benthic foraminifera suggest heightened biological productivity at the YD/Holocene transition off north Nordaustlandet³¹ and north off Kvitøya Trough, where palaeoproductivity at the time was estimated at 120 g cm² a⁻¹, approximately twice the present-day regional values⁴⁸. This regional palaeoproductivity increase was likely promoted by high insolation²⁷. The biologically productive MIZ was probably proximal to our study sites, though alternatively leads within the seasonal sea ice pack may have provided a suitable environment for open water algal growth⁴⁹.

From ~9.1 cal ka BP onwards, both our records show lower concentrations of individual biomarkers, including those produced by sea-ice diatoms and pelagic algae (Fig. 2), whereas ratio-based spring sea-ice concentrations increase and HBI T₂₅ remains low (Fig. 2). By ~8.3 cal ka BP, both sites are characterized by predominantly extensive SpSIC (consistently >50%). The seemingly low concentrations of individual biomarkers after ~9.1 cal ka BP are likely a result of a masking effect by their very high earlier concentrations during and after the YD (Fig. 2), in addition to individual HBIs suffering from variability in factors such as production, export, and preservation compared to ratio-based approaches^{50,51}. In fact, ratio-based methods, such as SpSIC and HBI T₂₅, show much better semi-quantitative calibrations (i.e., to measured spring sea-ice concentrations and spring chlorophyll-a values, respectively) than individual biomarkers^{44,51}. Our pattern of the early Holocene reduction of individual biomarkers following high YD and post-YD concentrations is in keeping with other regional records, including those in eastern Fram Strait²⁷ and the western Barents Sea²⁸. The concomitant increase in ratio-based SpSIC seen in our records after ~9.1 cal ka BP is furthermore in keeping with a regional trend towards more polar conditions influenced by Arctic surface waters that is observed across the region (Fig. 3), including subsurface and bottom water cooling from ~9 cal ka BP

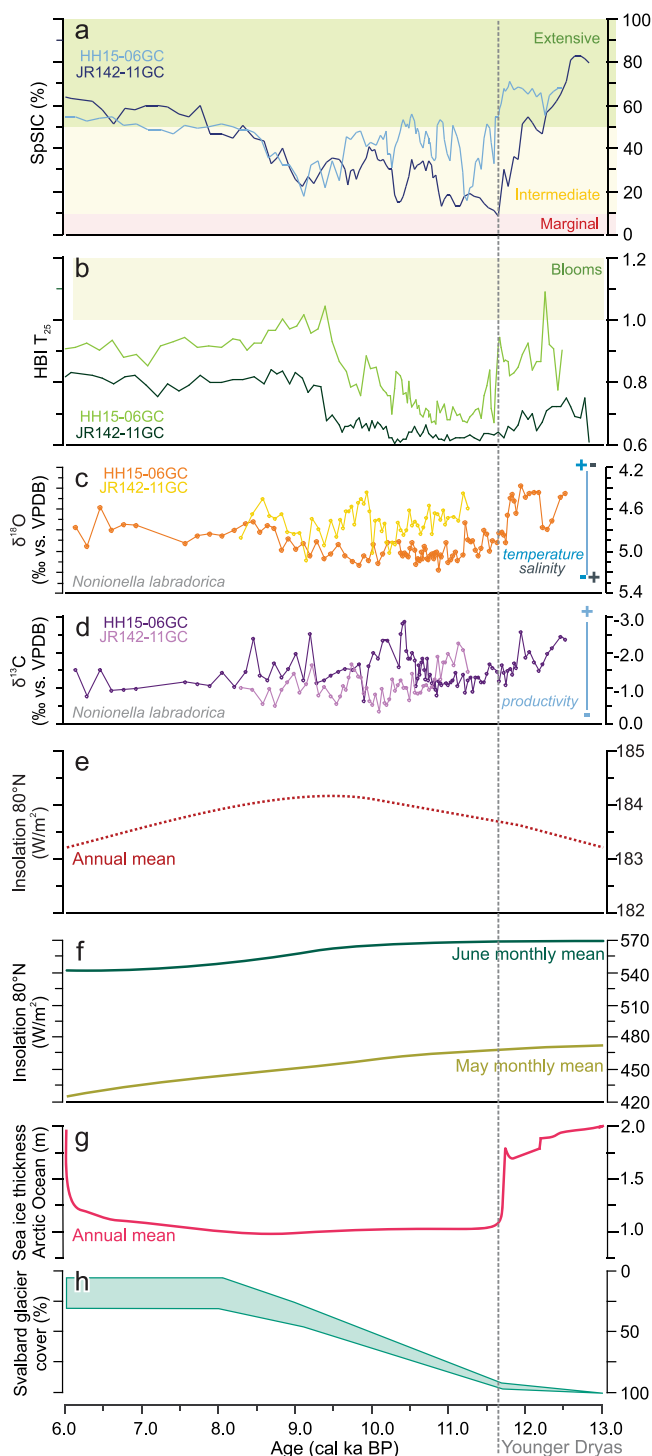


Fig. 3 Results of cores 11GC (JR142-11GC) and 06GC (HH15-06GC) in the context of other studies. **a** Biomarker-based spring sea-ice concentrations (SpSIC %), and **b** Marginal Ice Zone condition (HBI T_{25}) reconstructions are shown along with results on benthic foraminiferal stable isotopes of: **c** oxygen ($\delta^{18}\text{O}$), and **d** carbon ($\delta^{13}\text{C}$). Results of other relevant studies include insolation values¹⁶ for 80°N in terms of: **e** annual, and **f** monthly (May, June) means (in W m^{-2}). **g** Annual mean sea ice thicknesses for the Arctic Ocean from model simulations using dynamic surface albedo parameterization (normal simulation)¹⁵. **h** Percentage Svalbard glacier cover²⁵.

onwards^{23,52}. This signifies the end of the HTM on the northern Svalbard margin as both the insolation maximum and Atlantic Water inflow diminished. To the south of our sites, however, the end of the HTM may have been delayed, as indicated by increasing seasonal sea ice in Olga Basin after 5.9 cal ka BP²⁹ and the expansion of glaciers across Svalbard after ~6 cal ka BP²⁵.

Implications for ongoing climate warming. Atmosphere–ocean coupled general circulation models (CGCM/AOGCM) have demonstrated the possibility of perennial sea ice in the Arctic Ocean north of our core sites shifting to a seasonal sea-ice regime during the HTM¹⁵. Although driven by different factors during the HTM (heightened insolation then¹⁶ vs. greenhouse gas emissions today⁵³), such a scenario may be a possibility for a future Arctic Ocean⁵³, with marginal regions such as the Barents Sea shifting to open-water conditions year-round⁶. However, considerable uncertainties exist around model projections⁸, in part because the short period of sea-ice observations does not capture the internal variability of the system⁴. These factors hinder a sole reliance on model simulations to assess how sea ice will respond to continuing climate warming. This knowledge gap can, however, be bridged by geological data like those presented here, which use robust sea-ice proxies to elucidate warmer-than-present time periods at high temporal resolution.

Our results demonstrate that the northern Barents Sea margin was characterized by intermediate spring sea-ice concentrations at 11.7–9.1 cal ka BP during the HTM, when records in eastern Fram Strait²⁷, the western and north-central Svalbard Shelf²³, and the western Barents Sea²⁸ generally indicate substantially reduced or even absent sea ice, while northern areas like the Yermak Plateau were characterized by contemporaneous perennial sea ice³². The presence of open-water (phytoplankton) biomarkers, alongside those synthesized by sea-ice diatoms, in both cores, implies that the productive MIZ was nearby, located likely to the west of our study area. The situation to the south and east is less clear, however. Benthic foraminifera (diversities and assemblage composition) along with the presence of planktic foraminifera point to a relatively productive contemporaneous setting marked by reduced sea ice, heightened inflow of Atlantic-source water, and warm surface water conditions south of Kvitøya²⁰. Northwest of Kvitøya, Modern Analogue Technique transfer functions on dinoflagellate cysts imply ‘dense’ sea-ice cover most of the year (8–10 months per year) and reduced primary productivity during this time³⁴, while benthic foraminifera suggest enhanced primary productivity under Atlantic Water inflow, apparently denoting polynya development³³. These contrasts, together with the fact that the only other available HBI record from the area²⁹ covers the period from 9.5 cal ka BP onwards, make it at present impossible to determine if and how far south and east seasonal sea ice extended in the Barents Sea during the early Holocene.

The recent and ongoing decline in seasonal sea ice in the Barents Sea has been linked primarily to the increased inflow of oceanic heat via the northernmost extension of the Norwegian Atlantic Current (the West Spitsbergen Current, Fig. 1), which regulates sea-ice extent and particularly affects winter sea-ice cover^{42,54}. Such ‘Atlantification’ has also been implied during the HTM by palaeo-records in the Barents Sea, which show increased abundances of Atlantic-affiliated foraminiferal taxa along the Svalbard margin, especially in the west²³. An Atlantic Water signal is also apparent in our cores on the northwestern Svalbard shelf, which suggest that subsurface waters of Atlantic origin reached this high-latitude area during the early Holocene. Even so, this northward Atlantic inflow, in tandem with

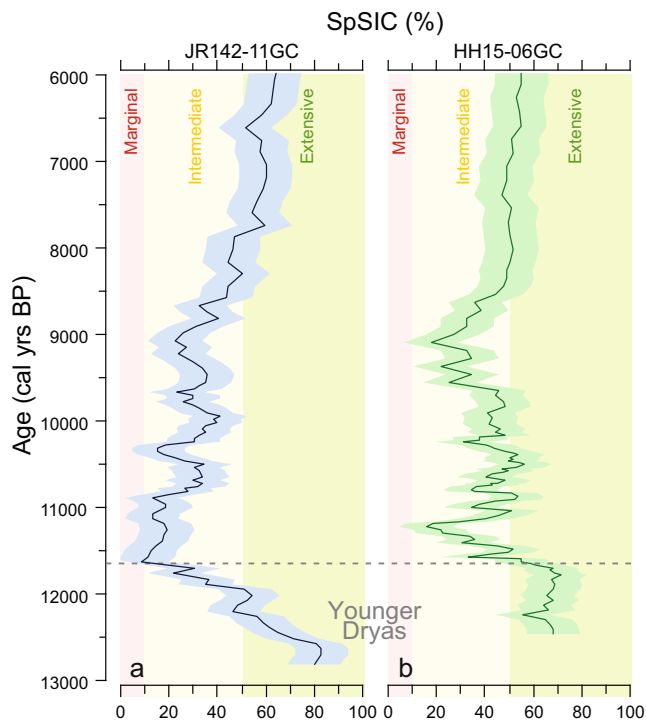


Fig. 4 Biomarker-based sea-ice reconstructions for cores 11GC (JR142-11GC) and 06GC (HH15-06GC). Spring sea-ice concentrations (SpSIC %) are shown for: **a** 11GC, and **b** 06GC in bold dark blue and dark green lines, respectively; error envelopes of RMSE (root mean square error) are denoted by lighter blue (11GC) and medium green (06GC). Sea-ice categories follow Köseoğlu et al.¹¹.

the warm HTM prevailing at the time, were apparently insufficient to result in fully open water conditions during spring. While oceanic heat has been recognized as an important factor in preventing the formation of sea ice in the Barents Sea at present⁴², its driving force may diminish in future, as changes in atmospheric circulation are likely to decrease Atlantic Water inflow into the Barents Sea⁵⁵. Nonetheless, increasing atmospheric temperatures driven by greenhouse gas emissions may still prevent sea-ice formation or cause substantial thinning of ice in the following season, given continuing ice-albedo feedbacks, especially if a threshold of oceanic absorption of summer solar radiation has already been crossed⁵⁶. It is also noteworthy that Northern Hemisphere sea ice appears to have persisted along the East Greenland coast (but not, noticeably, on the Yermak Plateau) during the Early Pliocene under warm global temperatures and high atmospheric CO₂ levels (380–400 ppm), although it is unclear whether it was produced in situ or transported into the area and trapped along the coast⁵⁷. Our results showing that sea ice persisted at 11.7–9.1 cal ka BP through the HTM are in keeping with model projections placing the sea-ice edge around the northern Barents Sea from the 2070s onwards; this is despite continuing Atlantic Water inflows and the feedbacks for sea-ice formation in subsequent seasons⁵⁵. One reason for the continuing presence of sea ice in the future may be water column stratification³⁷, an oceanographic setting also implied in our reconstructions. This suggests that if the warm Atlantic Water layer is sufficiently separated from the surface by a cold (and fresher) intermediate layer, such as Arctic Water flowing in from the north and east⁷, sea ice may continue to persist at high Arctic latitudes (>80°N) even in periods of warm climate. A continued freshwater supply, such as import of sea ice from the Arctic Ocean, may however be required to maintain this intermediate buffer and prevent vertical mixing^{42,43}. It is unclear whether and how fast the current deterioration of stratification

observed in the northern Barents Sea, a result of heat input to the intermediate layer and potentially signifying the shift from an Arctic towards an Atlantic domain⁴², would reverse under a future scenario of lessened Atlantic influence⁵⁵.

The Barents Sea is one of the most productive marginal seas of the Arctic Ocean and supports some of the World's most important and lucrative fish stocks⁵⁸. The recently observed physical shifts in the Arctic, including declining sea ice and increased ocean heat transport, have already been linked to biological changes, most notably considerably higher (>30%) annual net primary productivity since the late 1990s⁵⁹, earlier seasonal phytoplankton blooms⁶⁰, and algal blooming under relatively thin first year ice⁶¹. Our northern Barents Sea records confirm relatively productive surface water conditions at 11.7–9.1 cal ka BP during the HTM, characterized by high phytoplankton biomarker concentrations and low benthic foraminiferal δ¹³C values (Fig. 3). This corroborates the proposition that reduced sea-ice regimes are likely to promote higher biological productivity, especially through increasing light penetration which boosts phytoplankton growth¹, as long as vertical stratification still allows upwelling of nutrients⁶². Furthermore, if seasonal sea ice persists in the northern Barents Sea during periods of warmer climate, as indicated by our data, primary productivity may also increase within the sea ice (sympagic) ecosystem itself, especially under a thinning ice regime. In turn, this could contribute considerably to overall Arctic net primary productivity, as indicated by modern measurements⁶³. Although climatic amelioration and sea-ice change may boost primary productivity in the short-term, such changes in the overall physical system also have the potential to alter phytoplankton community structure and distribution, inevitably cascading through the foodweb to higher trophic levels both in the water column and in the benthos, with mixed (i.e., interacting positive and negative) effects for most key functional groups¹. The distribution of the commercially important Arctic cod (*Gadus morhua*) is closely tied to the inflow of Atlantic Water⁶⁴, and the species has been recently observed in waters northwest and north of Svalbard⁶⁵. However, the persistence of sea ice in the northeastern Barents Sea, as indicated by our reconstructions and by future projections⁵⁵, may curtail the expansion of Arctic cod into the high Arctic, as it does to other taxa such as haddock (*Melanogrammus aeglefinus*) via thermally limiting spawning capabilities⁶⁶. Lastly, continuing seasonal sea ice in the northern Barents Sea may also hinder marine transport via the Central Arctic Ocean or the so-called Northern Sea Route⁶⁷, as well as the extraction of natural resources such as hydrocarbon reserves¹.

In light of the present context of anthropogenically driven climate change and cryospheric deterioration, our results provide a vital perspective on the nuanced response of seasonal sea ice to increasingly warmer oceanic conditions by demonstrating that seasonal sea ice persisted in the northern Barents Sea between 11.7 and 9.1 cal ka BP through the HTM, and that the productive MIZ was located nearby. The warmer-than-present spring and summer conditions during this time, along with the inflow of subsurface Atlantic Water, were insufficient to cause sea-ice-free conditions, perhaps due to stratification efficiently buffering a warmer, saline subsurface from colder, fresher surface waters. As such, our reconstructions allow an important long-term perspective on sea ice beyond the short observational time period and provide data for constraining numerical models of future projections in warmer climates.

Methods

This study is based on two gravity cores (Fig. 1) collected in 2006 ('11GC', JR142-11GC⁶⁸: 81°04.90'N 28°55.60'E, 359 m water depth, 213 cm core length) and 2015 ('06GC', HH15-06GC: 80°32.60'N, 23°31.40'E, 320 m water depth, 445 cm core length). Each core was sampled at 1 cm intervals shortly after collection for HBI (highly branched isoprenoid) biomarkers in the interval focused on the YD chronozone and into the mid Holocene (JR142-11GC: 50–150 cm; HH15-06GC:

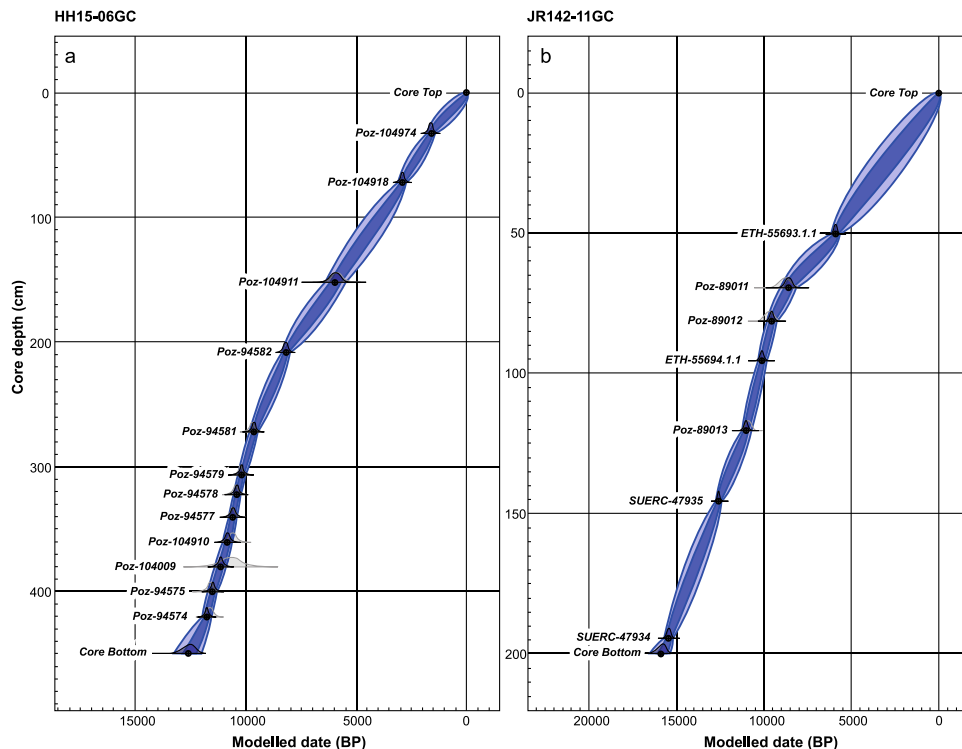


Fig. 5 Age-depth models for the cores used in this study. **a** core 06GC (HH15-06GC) and **b** core 11GC (JR142-11GC). Dark and light blue envelopes outline the 68% and 95% probability density ranges for each age-depth model, corresponding approximately to a one and two age standard deviation, respectively. Light grey curves show probability distributions (likelihood) for single dates in years before present (BP); their marginal modelled posterior distributions, which take into account the constructed age-depth model, are shown as dark grey curves. The median modelled ages of the time markers used are highlighted by black circles. For details on individual dates, refer to Table 1.

Table 1 Radiocarbon dates for cores 11GC (JR142-11GC) and 06GC (HH15-06GC).

Core depth (cm)	Laboratory code	Dated material	Conventional ¹⁴ C date ± 1σ (¹⁴ C a BP)	Calibrated age range (95.4%) (cal. a BP)	Median probability age (cal. a BP)
JR142-11GC					
50-51	ETH-55693.1.1	MBF	5803 ± 71	5670-6137	5900
50-51 (duplicate)	ETH-55693.3.1	BF: <i>N. labradorica</i>	5667 ± 137	5438-6106	5754
69-70	Poz-89011	BF: <i>N. labradorica</i>	8500 ± 240	8220-9386	8781
81-82	Poz-89012	BF: <i>N. labradorica</i>	9280 ± 140	9416-10,158	9756
95-96	ETH-55694.1.1	BF: <i>N. labradorica</i>	9557 ± 83	9816-10,401	10,120
95-96 (duplicate)	ETH-55694.3.1	BF: <i>N. labradorica</i>	9566 ± 187	9563-10,632	10,123
120-121	Poz-89013	BF: <i>N. labradorica</i>	10,100 ± 100	10,556-11,175	10,873
145-146	SUERC-47935	MBF	11,326 ± 39	12,444-12,722	12,591
194-195	SUERC-47934	MBF	13,601 ± 42	15,184-15,661	15,422
HH15-06GC					
32-33	Poz-104974	MBF	2305 ± 35	1450-1790	1619
72-73	Poz-104918	MBF	3370 ± 35	2749-3092	2914
152-153	Poz-104911	MBF	5810 ± 250	5338-6444	5908
208-209	Poz-94582	BF: <i>N. labradorica</i>	8030 ± 50	8031-8370	8218
272-273	Poz-94581	BF: <i>N. labradorica</i>	9260 ± 50	9503-9939	9701
306-307	Poz-94579	BF: <i>N. labradorica</i>	9630 ± 50	10,008-10,440	10,221
322-323	Poz-94578	BF: <i>N. labradorica</i>	9820 ± 50	10,240-10,661	10,456
340-341	Poz-94577	BF: <i>N. labradorica</i>	9900 ± 50	10,321-10,796	10,573
360-361	Poz-104910	MBF	9920 ± 100	10,272-10,992	10,609
380-381	Poz-104909	MBF	9970 ± 370	9651-11,736	10,694
400-401	Poz-94575	BF: <i>N. labradorica</i>	10,640 ± 50	11,346-869	11,619
420-421	Poz-94574	BF: <i>N. labradorica</i>	10,640 ± 50	11,346-869	11,619

All dates were calibrated in CALIB 8.2⁷² using the MARINE20 calibration curve⁷³ and a ΔR of 105 ± 24 yr applicable to the Barents Sea (Bondevik & Gulliksen in Mangerud et al. ⁷⁴). ‘MBF’ denotes mixed benthic foraminifera; ‘BF’ refers to benthic foraminifera. Laboratory codes: ETH = Laboratory of Ion Beam Physics at ETH, Zürich, Switzerland; Poz = Poznań Radiocarbon Laboratory, Poznań, Poland; SUERC = SUERC AMS Laboratory, NERC Radiocarbon Facility, East Kilbride, UK.

152–445 cm). The sediments were subsequently freeze-dried and homogenized with pestle and mortar. About 2.5 g of each sample was processed for HBIs according to a slightly adapted method of the standard procedure⁶⁹. Each batch of sediment samples ($n = 10$ –16) included a procedural blank and an in-house reference sediment sample containing HBIs of interest and with known concentrations. The reference sediment was obtained by homogenizing material from a piston core taken from Barrow Strait in the central Canadian Arctic in 2005⁷⁰. An internal standard (9-octylheptadec-8-ene (9-OHD); 100 ng) was added to each sample prior to extraction, which encompassed the following steps: addition of 6 ml potassium hydroxide (KOH, Fisher Scientific) solution (5 g KOH in 9:1 methanol:milliQ water), heating of sediment-KOH mixture at 70 °C for 1 h, addition of hexane (Rathburn Chemicals) in three steps (6 ml total) and centrifugation (2 min at 2500 rpm), collection of hexane by pipetting into new vials, and removal of hexane under gentle N₂ stream (25 °C). The sample was then purified by re-dissolving the extract in hexane (6 ml) and running it through conditioned (hexane) silica columns (60–200 µm, ca. 0.5 g, Fisher Scientific), followed by the removal of hexane under gentle N₂ stream (25 °C). An additional step of purification was added to the HBI protocol by re-dissolving the dried extract in hexane (3 ml) and running it through silver-ion (Ag-Ion, Discovery[®]; ca. 0.1 g) columns⁷¹. Subsequently the extract was concentrated by removing most of the solvent under a gentle stream of N₂ (25 °C) and transferred into smaller vials. HBIs were analysed by gas chromatography–mass spectrometry (GC-MS, Agilent 7890 gas chromatograph equipped with the HP5MS fused-silica column (30 m; 0.25 mm film thickness; 0.25 mm internal diameter)) coupled to an Agilent 5975 series mass selective detector, and peaks of IP₂₅, IPSO₂₅, HBI III and HBI IV were identified and quantified in the software MSD ChemStation (GC retention indices (RIHP5MS) = 2081, 2082, 2044 and 2091 for IP₂₅, IPSO₂₅, HBI III and HBI IV, respectively). Peak values were translated into HBI concentrations (ng HBI per g of dry sediment) by their relation to peak areas and sediment masses vis-à-vis the internal standard and the reference sediment. HBI concentrations (ng g⁻¹) were further used to calculate spring sea-ice concentrations (SpSIC) and the HBI T₂₅ index (a measure of phytoplankton blooms at the productive MIZ) using the following formulae⁴⁴.

$$\text{SpSIC}(\%) = \left(\left(\frac{\text{IP}_{25}}{((\text{IP}_{25} + \text{HBI III}) \times 0.63)} \right) - 0.0692 \right) / 0.0107$$

$$\text{HBI T}_{25} = \frac{\left(\frac{\text{HBI III}}{(\text{HBI III} + \text{HBI IV})} \right)}{0.62}$$

SpSIC categories follow the ones defined by Köseoglu et al.¹¹: 0–10% = marginal; 10–50% = intermediate; 50–100% = extensive. To permit clear site comparisons, HBI-based SpSIC reconstructions are shown without error envelope (RMSE, root mean square error) in figures 2 and 3, but are displayed with error envelopes in Fig. 4.

For foraminiferal stable isotopes, δ¹⁸O and δ¹³C were measured on 15–20 individuals of pristine *Nonionella labradorica* per sample with an automatic Finnigan MAT 253 mass spectrometer coupled to an automated Kiel device at the stable isotope laboratory (FARLAB) of the University of Bergen. Sampling intervals focused on the same core sections as biomarkers; due to the low abundance of foraminifera in JR142-11GC, stable isotopes are not available for some of the parts of this core. Results are given relative to the Vienna Pee Dee Belemnite (VPDB) standard, without corrections applied for vital or ice volume effects. Biomarker and stable isotope data were plotted in the C2 software⁷².

Radiocarbon dates were measured on mixed (predominantly *Cassidulina reniforme*, *Elphidium excavatum* f. *clavata*, *N. labradorica*) or monospecific (*N. labradorica*) benthic foraminifera; nine dates (including two duplicates) are available for JR142-11GC and 12 dates are available for HH15-06GC. All dates were calibrated in CALIB 8.2⁷³ using the MARINE20 calibration curve⁷⁴ and a regional radiocarbon reservoir offset (ΔR) of 105 ± 24 yr applicable to the Barents Sea (Bondevik & Gulliksen in Mangerud et al.⁷⁵). The age depth models for the cores (Fig. 5) were developed with Bayesian technique OxCal 4.4⁷⁶ using a Poisson deposition model. The estimates of the model parameter k of 0.3 (HH15-06GC) and 0.5 (JR142-11GC)—number of deposition events per unit length, also reflective of fluctuations in the sedimentation rate—are derived by the age model fit optimization procedure⁷⁶. The ages of the core tops for the modelling were set to U [1900, 2006] and U [1900, 2015] for JR142-11GC and HH15-06GC, respectively, with U standing for the uniform probability distribution function. Since the core sections younger than 6 kyr BP are not considered in the present paper, this specific choice has no influence on the results presented here, as long as it is based on the inferred core-averaged sedimentation rate (Table 1).

Data availability

Data generated in this study are available at <https://doi.org/10.21334/npolar.2021.435e2671>.

Received: 2 January 2021; Accepted: 18 May 2021;

Published online: 15 June 2021

References

- Meredith, M. et al. Polar regions. In: *IPCC Special Report on the Ocean and Cryosphere in a Changing Climate* (eds Potrner, H.-O. et al.) 203–320 (2019).
- Stroeve, J. C. et al. The Arctic's rapidly shrinking sea ice cover: a research synthesis. *Clim. Change* **110**, 1005–1027 (2012).
- Francis, J. A., Vavrus, S. J. & Cohen, J. Amplified Arctic warming and mid-latitude weather: new perspectives on emerging connections. *Wiley Interdiscip. Rev. Clim. Chang.* **8**, e474 (2017).
- Notz, D. How well must climate models agree with observations? *Philos. Trans. R. Soc. A* **373**, 20140164 (2015).
- Jahn, A., Kay, J. E., Holland, M. M. & Hall, D. M. How predictable is the timing of a summer ice-free Arctic? *Geophys. Res. Lett.* **43**, 9113–9120 (2016).
- Onarheim, I. H. & Årthun, M. Toward an ice-free Barents Sea. *Geophys. Res. Lett.* **44**, 8387–8395 (2017).
- Smedsrud, L. H. et al. The role of the Barents Sea in the arctic climate system. *Rev. Geophys.* **51**, 415–449 (2013).
- Stroeve, J. & Notz, D. Insights on past and future sea-ice evolution from combining observations and models. *Glob. Planet. Change* **135**, 119–132 (2015).
- Dai, A., Luo, D., Song, M. & Liu, J. Arctic amplification is caused by sea-ice loss under increasing CO₂. *Nat. Commun.* **10**, 121 (2019).
- Comiso, J. C. & Hall, D. K. Climate trends in the Arctic as observed from space. *WIREs Clim. Change* **5**, 389–409 (2014).
- Köseoglu, D. et al. Complementary biomarker-based methods for characterising Arctic sea ice conditions: a case study comparison between multivariate analysis and the PIP₂₅ index. *Geochim. Cosmochim. Acta* **222**, 406–420 (2018).
- Jakobsson, M., Long, A., Ingólfsson, Ó., Kjær, K. H. & Spielhagen, R. F. New insights on Arctic Quaternary climate variability from palaeo-records and numerical modeling. *Quat. Sci. Rev.* **29**, 3349–3358 (2010).
- Bova, S., Rosenthal, Y., Liu, Z., Godard, S.P. & Yan, M. Seasonal origin of the thermal maxima at the Holocene and the last interglacial. *Nature* **589**, 548–553 (2021).
- Perovich, D. K. & Polashenski, C. Albedo evolution of seasonal Arctic sea ice. *Geophys. Res. Lett.* **39**, L08501 (2012).
- Stranne, C., Jakobsson, M. & Björk, G. Arctic Ocean perennial sea ice breakdown during the Early Holocene Insolation Maximum. *Quat. Sci. Rev.* **92**, 123–132 (2014).
- Berger, A. Long-term variations of daily insolation and Quaternary climatic changes. *J. Atmos. Sci.* **35**, 2362–2367 (1978).
- Rasmussen, T. L. et al. Paleooceanographic evolution of the SW Svalbard margin (76°N) since 20,000 ¹⁴C yr BP. *Quat. Res.* **67**, 100–114 (2007).
- Aagaard-Sørensen, S., Husum, K., Hald, M. & Knies, J. Paleooceanographic development in the SW Barents Sea during the Late Weichselian-Early Holocene transition. *Quat. Sci. Rev.* **29**, 3442–3456 (2010).
- Skirbekk, K., Klitgaard-Kristensen, D., Rasmussen, T. L., Koç, N. & Forwick, M. Holocene climate variations at the entrance to a warm Arctic fjord: evidence from Kongsfjorden trough. *Svalbard. Geol. Soc. Lond. Spec. Publ.* **344**, 289–304 (2010).
- Klitgaard Kristensen, D. K., Rasmussen, T. L. & Koç, N. Palaeoceanographic changes in the northern Barents Sea during the last 16 000 years—new constraints on the last deglaciation of the Svalbard-Barents Sea Ice Sheet. *Boreas* **42**, 798–813 (2013).
- Blaschek, M., Renssen, H., Kissel, C. & Thornalley, D. Holocene North Atlantic Overturning in an atmosphere-ocean-sea ice model compared to proxy-based reconstructions. *Paleoceanography* **30**, 1503–1524 (2015).
- Ganopolski, A. & Brovkin, V. Simulation of climate, ice sheets and CO₂ evolution during the last four glacial cycles with an Earth system model of intermediate complexity. *Clim. Past* **13**, 1695–1716 (2017).
- Rasmussen, T. L. et al. Spatial and temporal distribution of Holocene temperature maxima in the northern Nordic seas: interplay of Atlantic-, Arctic- and polar water masses. *Quat. Sci. Rev.* **92**, 280–291 (2014).
- Salvigsen, O., Forman, S. L. & Miller, G. H. Thermophilous molluscs on Svalbard during the Holocene and their paleoclimatic implications. *Polar Res.* **11**, 1–10 (1992).
- Farnsworth, W. R. et al. Holocene glacial history of Svalbard: status, perspectives and challenges. *Earth Sci. Rev.* **208**, 103249 (2020).
- Allaart, L. et al. Late Quaternary glacier and sea-ice history of northern Wijdefjorden, Svalbard. *Boreas* **49**, 417–437 (2020).
- Müller, J. & Stein, R. High-resolution record of late glacial and deglacial sea ice changes in Fram Strait corroborates ice-ocean interactions during abrupt climate shifts. *Earth Planet. Sci. Lett.* **403**, 446–455 (2014).
- Berben, S., Husum, K., Cabedo-Sanz, P. & Belt, S. T. Holocene sub-centennial evolution of Atlantic water inflow and sea ice distribution in the western Barents Sea. *Clim. Past* **10**, 181–198 (2014).
- Berben, S. M. P., Husum, K., Navarro-Rodriguez, A., Belt, S. T. & Aagaard-Sørensen, S. Semi-quantitative reconstruction of early to late Holocene spring

- and summer sea ice conditions in the northern Barents Sea. *J. Quat. Sci.* **32**, 587–603 (2017).
30. Werner, K. et al. Holocene sea subsurface and surface water masses in the Fram Strait – comparisons of temperature and sea-ice reconstructions. *Quat. Sci. Rev.* **147**, 194–209 (2016).
 31. Chauhan, T., Rasmussen, T. L. & Noormets, R. Palaeoceanography of the Barents Sea continental margin, north of Nordaustlandet, Svalbard, during the last 74 ka. *Boreas* **45**, 76–99 (2016).
 32. Kremer, A. et al. Changes in sea ice cover and ice sheet extent at the Yermak Plateau during the last 160 ka: reconstructions from biomarker records. *Quat. Sci. Rev.* **182**, 93–108 (2018).
 33. Ivanova, E. et al. Postglacial variations in Atlantic Water inflow, iceberg calving and sea ice conditions in the northwestern Barents Sea. *Quat. Res.* **92**, 430–449 (2019).
 34. Brice, C., de Vernal, A., Ivanova, E., van Bellen, S. & van Nieuwenhove, N. Palynological evidence of sea-surface conditions in the Barents Sea off northeast Svalbard during the postglacial period. *Quat. Res.* **1–15**; <https://doi.org/10.1017/qua.2020.2> (2020).
 35. Hogan, K. A. et al. Subglacial sediment pathways and deglacial chronology of the northern Barents Sea Ice Sheet. *Boreas* **46**, 750–771 (2017).
 36. Ślubowska, M. A., Koç, N., Rasmussen, T. L. & Klitgaard-Kristensen, D. Changes in the flow of Atlantic water into the Arctic Ocean since the last deglaciation: evidence from the northern Svalbard continental margin, 80°N. *Paleoceanography* **20**, PA4014 (2005).
 37. Renner, A. H. H. et al. Variability and redistribution of heat in the Atlantic Water boundary current north of Svalbard. *J. Geophys. Res. Oceans* **123**, 6373–6391 (2018).
 38. Mackensen, A. & Hald, M. *Cassidulina teretis* Tappan and *C. laevigata* d’Orbigny: their modern and late Quaternary distribution in northern seas. *J. Foramin. Res.* **18**, 16–24 (1988).
 39. Cage, A. G., Pieńkowski, A. J., Jennings, A., Knudsen, K.-L. & Seidenkrantz, M.-S. Comparative analysis of six common foraminiferal species of the genera *Cassidulina*, *Paracassidulina*, and *Islandiella* from the Arctic–North Atlantic domain. *J. Micropalaeontology* **40**, 37–60 (2021).
 40. Jennings, A. & Helgadóttir, G. Foraminiferal assemblages from the fjords and shelf of eastern Greenland. *J. Foramin. Res.* **24**, 123–144 (1994).
 41. Lubinski, D. J., Polyak, L. V. & Forman, S. L. Freshwater and Atlantic water inflows to the deep northern Barents and Kara seas since ca. 13 ¹⁴C ka: foraminifera and stable isotopes. *Quat. Sci. Rev.* **20**, 1851–1879 (2001).
 42. Lind, S., Ingvaldsen, R. B. & Furevik, T. Arctic warming hotspot in the northern Barents Sea linked to declining sea-ice import. *Nature Clim. Change* **8**, 634–639 (2018).
 43. Lind, S., Ingvaldsen, R. B. & Furevik, T. Arctic layer salinity controls heat loss from deep Atlantic layer in seasonally ice-covered areas of the Barents Sea. *Geophys. Res. Lett.* **43**, 5233–5242 (2016).
 44. Belt, S. T., Smik, L., Köseoglu, D., Knies, J. & Husum, K. A novel biomarker-based proxy for the spring phytoplankton bloom in Arctic and sub-arctic settings – HBI T₂₅. *Earth Planet. Sci. Lett.* **523**, 115703 (2019).
 45. Belt, S. T. et al. Identification of paleo Arctic winter sea ice limits and the marginal ice zone: optimised biomarker-based reconstructions of late Quaternary Arctic sea ice. *Earth Planet. Sci. Lett.* **431**, 127–139 (2015).
 46. Hald, M. et al. Variations in temperature and extent of Atlantic Water in the northern North Atlantic during the Holocene. *Quat. Sci. Rev.* **26**, 3423–3440 (2007).
 47. Cabedo-Sanz, P., Belt, S. T., Knies, J. & Husum, K. Identification of contrasting seasonal sea ice conditions during the Younger Dryas. *Quat. Sci. Rev.* **79**, 74–86 (2013).
 48. Wollenburg, J. E., Knies, J. & Mackensen, A. High-resolution paleoproductivity fluctuations during the past 24 kyr as indicated by benthic foraminifera in the marginal Arctic Ocean. *Palaeogeogr. Palaeoclimatol. Palaeoecol.* **204**, 209–238 (2004).
 49. Assmy, P. et al. Leads in Arctic pack ice enable early phytoplankton blooms below snow-covered sea ice. *Sci. Rep.* **7**, 40850 (2017).
 50. Cabedo-Sanz, P., Smik, L. & Belt, S. T. On the stability of various highly branched isoprenoid (HBI) lipids in stored sediments and sediment extracts. *Org. Geochem.* **97**, 74–77 (2016).
 51. Belt, S. T. Source-specific biomarkers as proxies for Arctic and Antarctic sea ice. *Org. Geochem.* **125**, 277–298 (2018).
 52. Risebrobakken, B. et al. Early Holocene temperature variability in the Nordic Seas: the role of oceanic heat advection versus changes in orbital forcing. *Paleoceanography* **26**, PA4206 (2011).
 53. Collins, M. et al. Long-term climate change: projections, commitments and irreversibility. In *Climate Change 2013: The Physical Science Basis. Contribution of Working Group I to the Fifth Assessment Report of the Intergovernmental Panel on Climate Change* (eds Stocker, T. F. et al.) 1029–1136 (Cambridge University Press, 2013).
 54. Li, D., Zhang, R. & Knutson, T. R. On the discrepancy between observed and CMIP5 multi-model simulated Barents Sea winter sea ice decline. *Nat. Commun.* **8**, 14991 (2017).
 55. Årthun, M., Eldevik, T. & Smedsrud, L. H. The role of Atlantic heat transport in future arctic winter sea ice loss. *J. Climate* **32**, 3327–3341 (2019).
 56. Serreze, M. C. & Francis, J. A. The Arctic amplification debate. *Clim. Change* **76**, 241–264 (2006).
 57. Clotten, C. et al. On the causes of Arctic sea ice in the warm Early Pliocene. *Sci. Rep.* **9**, 989 (2019).
 58. Hunt, G. L. Jr. et al. The Barents and Chukchi Seas: comparison of two Arctic shelf ecosystems. *J. Mar. Syst.* **109–110**, 43–68 (2012).
 59. Arrigo, K. R. & van Dijken, G. L. Continued increases in Arctic Ocean primary production. *Prog. Oceanogr.* **136**, 60–70 (2015).
 60. Kahru, M., Brotas, V., Manzano-Sarabia, M. & Mitchell, B. G. Are phytoplankton blooms occurring earlier in the Arctic? *Glob. Chang. Biol.* **17**, 1733–1739 (2011).
 61. Horvat, C. et al. The frequency and extent of sub-ice phytoplankton blooms in the Arctic Ocean. *Sci. Adv.* **3**, e1601191 (2017).
 62. Nummelin, A., Ilicak, M., Li, C. & Smedsrud, L. H. Consequences of future increased Arctic runoff on Arctic Ocean stratification, circulation, and sea ice cover. *J. Geophys. Res. Oceans* **121**, 617–637 (2016).
 63. Song, H. J. et al. In-situ measured primary productivity of ice algae in Arctic sea ice floes using a new incubation method. *Ocean Sci. J.* **51**, 387–396 (2016).
 64. Årthun, M. et al. Climate based multi-year predictions of the Barents Sea cod stock. *PLoS ONE* **13**, e0206319 (2018).
 65. Ingvaldsen, R. B., Gjosæter, H., Ona, E. & Michalsen, K. Atlantic cod (*Gadus morhua*) feeding over deep water in the high Arctic. *Polar Biol.* **40**, 2105–2111 (2017).
 66. Landa, C. S. et al. Recruitment, distribution boundary and habitat temperature of an arcto-boreal gaidoid in a climatically changing environment: a case study on Northeast Arctic haddock (*Melanogrammus aeglefinus*). *Fish. Oceanogr.* **23**, 506–520 (2014).
 67. Melia, N., Haines, K. & Hawkins, E. Sea ice decline and 21st century trans-Arctic shipping routes. *Geophys. Res. Lett.* **43**, 9720–9728 (2016).
 68. Hogan, K. A. et al. Submarine landforms and ice-sheet flow in the Kvitøya Trough, northwestern Barents Sea. *Quat. Sci. Rev.* **29**, 3545–3562 (2010).
 69. Belt, S. T. et al. A reproducible method for the extraction, identification and quantification of the Arctic sea ice proxy IP₂₅ from marine sediments. *Anal. Methods* **4**, 705–7013 (2012).
 70. Vare, L., Massé, G., Gregory, T. R., Smart, C. W. & Belt, S. T. Sea ice variations in the central Canadian Arctic Archipelago during the Holocene. *Quat. Sci. Rev.* **28**, 1354–1366 (2009).
 71. Cabedo Sanz, P. Identification of Variability in Sub-Arctic Sea Ice Conditions During the Younger Dryas and Holocene. Unpublished PhD thesis, University of Plymouth (2013).
 72. Juggins, S. C2 Version 1.5 user guide. Software for Ecological and Palaeoecological Data Analysis and Visualisation (Newcastle University, Newcastle upon Tyne, UK, 2007).
 73. Stuiver, M., Reimer, P. J. & Reimer, R. W. CALIB 8.2 [WWW program] <http://calib.org> (2020).
 74. Heaton, T. J. et al. Marine20 - the marine radiocarbon age calibration curve (0–55,000 Cal bp). *Radiocarbon* **62**, 779–820 (2020).
 75. Mangerud, J., Bondevik, S., Gulliksen, S., Hufthammer, A. K. & Høisæter, T. Marine ¹⁴C reservoir ages for 19th century whales and molluscs from the North Atlantic. *Quat. Sci. Rev.* **25**, 3228–3245 (2006).
 76. Bronk Ramsey, C. Bayesian analysis of radiocarbon dates. *Radiocarbon* **51**, 337–360 (2009).
 77. National Snow and Ice Data Center (NSIDC), <https://nsidc.org/> (2016).

Acknowledgements

This paper is a contribution to the Nansen Legacy Project (Norwegian Research Council project 276730). We acknowledge funding from the Norwegian Research Council, the Norwegian Polar Institute, and the HOLIS project funded by the Norwegian Ministry of Climate and Environment through the Fram Centre (Project no. 6622/299). J.K. and D.K. acknowledge funding from the Norwegian Research Council (Project no. 223259). FARLAB is supported by RCN project 245907. Svetlana Divina is thanked for assisting with the laboratory work, Oddveig Øien Ørvoll for providing the map, and Mark Furze for helping with the figures. We are grateful to the three reviewers whose comments improved the manuscript.

Author contributions

K. Husum designed the research and obtained research funding for this work together with D.D.; A.J.P. and K. Husum conceptualized the paper and wrote the manuscript, with substantial input from S.T.B., U.N. and D.D.; S.T.B. supervised biomarker analyses and data interpretation by D.K. and L.S.; U.N. conducted stable isotope analyses; D.D. constructed the age–depth models; J.K. contributed to discussions on data and interpretation; K. Hogan provided core materials and radiocarbon dates; and R.N. provided core materials. All authors contributed to data interpretation and manuscript writing.

Competing interests

The authors declare no competing interests.

Additional information

Correspondence and requests for materials should be addressed to A.J.P.

Peer review information *Communications Earth & Environment* thanks the anonymous reviewers for their contribution to the peer review of this work. Primary handling editors: Sze Ling Ho, Joe Aslin and Clare Davis.

Reprints and permission information is available at <http://www.nature.com/reprints>

Publisher's note Springer Nature remains neutral with regard to jurisdictional claims in published maps and institutional affiliations.



Open Access This article is licensed under a Creative Commons Attribution 4.0 International License, which permits use, sharing, adaptation, distribution and reproduction in any medium or format, as long as you give appropriate credit to the original author(s) and the source, provide a link to the Creative Commons license, and indicate if changes were made. The images or other third party material in this article are included in the article's Creative Commons license, unless indicated otherwise in a credit line to the material. If material is not included in the article's Creative Commons license and your intended use is not permitted by statutory regulation or exceeds the permitted use, you will need to obtain permission directly from the copyright holder. To view a copy of this license, visit <http://creativecommons.org/licenses/by/4.0/>.

© The Author(s) 2021